

Evolution of angular-resolved rate of Thomson scattering in intense laser fields

Ying Shen(申颖), Xianghe Ren(任向河), and Jingtao Zhang(张敬涛)
Citation: Chin. Phys. B, 2026, 35 (**1**): 014203. DOI: 10.1088/1674-1056/ade1bf
http://cpb.iphy.ac.cn; http://iopscience.iop.org/cpb

What follows is a list of articles you may be interested in

Phase controlled single photon transport in giant atoms coupling to one-dimensional waveguide

Yan-Yan Song(宋艳艳), Yao Zang(臧耀), Yunning Lu(路云宁), Zhao Liu(刘兆), Xiao-San Ma(马小三), and Mu-Tian Cheng(程木田)
Chin. Phys. B, 2025, 34 (**12**): 124206. DOI: 10.1088/1674-1056/ade8df

Tunable magnomechanically and optomechanically induced transparency in a cavity opto-magnomechanical system

Ke Di(邸克), Huarong Xia(夏华容), Wenting Diao(刁文婷), Chunxiao Cai(蔡春晓), Wenhai Yang(杨文海), Yulian Qin(秦瑜莲), Ziting Liao(廖子婷), Yucan He(何钰灿), and Jiajia Du(杜佳佳)
Chin. Phys. B, 2025, 34 (**7**): 074201. DOI: 10.1088/1674-1056/adc18f

Quantitative determination of modal photon number density spectrum in arbitrary dielectric structures with a quantum emitter

Li-Heng Chen(陈立恒), Fengfeng Luo(罗凤凤), and Yonggui Gao(高勇贵)
Chin. Phys. B, 2025, 34 (**4**): 044204. DOI: 10.1088/1674-1056/adb262

Modulation of Bessel-like vector vortex beam using the resonant magneto-optical effect in rubidium vapor

Yan Ma(马燕), Xin Yang(杨欣), Hong Chang(常虹), Ming-Tao Cao(曹明涛), Xiao-Fei Zhang(张晓斐), Rui-Fang Dong(董瑞芳), and Shou-Gang Zhang(张首刚)
Chin. Phys. B, 2025, 34 (**2**): 024202. DOI: 10.1088/1674-1056/ad9c43

Laser parameters affecting the asymmetric radiation of the electron in tightly focused intense laser pulses

Xing-Yu Li(李星宇), Wan-Yu Xia(夏婉瑜), You-Wei Tian(田友伟), and Shan-Ling Ren(任山令)
Chin. Phys. B, 2023, 32 (**12**): 124205. DOI: 10.1088/1674-1056/acd3dd

---

Evolution of angular-resolved rate of Thomson scattering in intense laser fields

Ying Shen(申颖)[1], Xianghe Ren(任向河)[2], and Jingtao Zhang(张敬涛)[1,†]

[1] *Department of Physics, Shanghai Normal University, Shanghai* 200234, *China*
[2] *International School for Optoelectronic Engineering, QiLu University of Technology (Shandong Academy of Sciences), Jinan* 250353, *China*

(Received 3 March 2025; revised manuscript received 5 June 2025; accepted manuscript online 6 June 2025)

By employing a full quantum theory of electron–photon scattering in intense laser fields, we calculate the angular-resolved radiation rate of the fundamental wave in Thomson scattering. We investigate the dependence of radiation rate on Euler angles and elucidate the underlying physical mechanism. The figure-8 profile of the radiation rate within the polarization plane is validated, while its evolution with respect to laser intensity and electron momentum is illustrated. Our findings reveal that in lower-intensity laser fields and for slow electron motion, the angular-resolved radiation rate exhibits distinct dipole emission characteristics. However, significant changes are observed at high laser intensities and/or large electron momenta, leading to pronounced alterations in the angular-resolved radiation rate. Remarkably similar variation patterns can be achieved by proportionally adjusting both laser intensity and electron momentum.

Keywords: Thomson scattering, full quantum theory, relativistic effects, angular-resolved scattering rate

PACS: 42.50.Ct, 42.68.Mj, 03.65.Nk, 41.60.Dk

DOI: 10.1088/1674-1056/ade1bf **CSTR:** 32038.14.CPB.ade1bf

1. Introduction

Thomson scattering refers to the scattering process where a free electron interacts with electromagnetic waves, as proposed by Thomson.[1] In this process, the oscillation of the free electron results in the emission of secondary electromagnetic waves. In intense laser fields, Thomson scattering serves as a valuable source for generating photons of extremely short wavelengths, such as gamma rays and extreme ultraviolet lights.[2–5] Due to the widespread utilization of these high-energy photons in fundamental research and practical applications, Thomson scattering has emerged as prominent subject within intense laser physics and has been extensively investigated over the past few decades.[6–15]

In the presence of intense laser fields, an electron can absorb one or more photons and subsequently emit a new photon. When only one photon is absorbed, the newly generated photon has the same frequency as the driving field, which is referred to as linear Thomson scattering (LTS). When multiple photons are absorbed, it is termed as nonlinear Thomson scattering (NTS).[16,17] The radiation emitted during the LTS process is generally considered as the dipole emission resulting from the acceleration caused by the time-varying force exerted by the laser field on the electron. Similarly, the second harmonics is regarded as the quadrupole radiation[9] and so on. Both LTS and NTS processes occur simultaneously in intense laser fields with high-frequency radiations gradually becoming dominant as laser intensity increases.[9,18–21]

The angular-resolved scattering rate provides a direct measure of the scattering rate by recording the emitted photons during scattering. Its profile indicates the relative variation with respect to azimuthal or scattering angles. Studying on the angular-resolved rate offers a convenient tool for elucidating variation mechanisms under identical conditions, thereby serving as a valuable means for identifying scattering mechanisms. Following the initial observation of several low-order harmonics in Thomson scattering,[9,10] significant attention was drawn towards angular-resolved rates, leading to continuous observations reported under various conditions.[21–24]

The angular-resolved scattering rate in the LTS process, referred to as the angular-distribution of the fundamental radiation (ADF), is of great importance. The ADF profiles vary with the electron momentum and the intensity of the driving field, which presents an indicative of electron motion in various laser fields. When the laser intensity is low, the electron moves classically in the laser field, and the ADFs exhibit a doughnut profile, indicating the dipole emission features from the oscillating electron. The electron speed increases with the intensity of the driving field, and hence the relativistic effect becomes distinctive gradually as the peak intensity exceeding 10^{17} W/cm^2. Consequently, the ADF profile exhibit non-dipole features in intense laser fields, such as the asymmetry observed in the figure-8 profile.[22] The observed ADF lacks symmetry about both the x-axis and the y-axis in the polarization plane. Although this asymmetry is relatively weak and has not garnered significant attention, its origin remains un-

†Corresponding author. E-mail: jtzhang@shnu.edu.cn

© 2026 Chinese Physical Society and IOP Publishing Ltd. All rights, including for text and data mining, AI training, and similar technologies, are reserved.

known, and how it can become more pronounced remains an open question. Furthermore, understanding how relativistic effects influence Thomson scattering dynamics in intense laser fields represents an intriguing area of investigation.

In a recent paper, we employed a comprehensive quantum treatment of the intense laser field and developed a rigorous quantum theory of electron–photon scattering.[25] In contrast to classical approaches that consider the laser light as a classical field, our approach treats it as a fully quantized field where photons are well-defined entities. By utilizing the quantum-field Volkov state derived by Guo *et al.*,[26] we obtain an analytical expression for the scattering probability. Based on this derived formula, we conducted an extensive investigation into the angular-resolved rate of scattered photons. The calculated ADHs exhibit significantly improved agreement with recent experimental data,[27] and also predict many features for further observations. This approach applies to electron–photon scattering in intense laser fields of arbitrary intensity.

This paper employs the derived analytical formula to examine the ADFs in various laser pulses with an emphasis on the evolution of ADFs in relation to laser intensity and electron momentum. We concentrate on the LTS process in longer laser pulses which can be treated as single-mode plane waves. When the pulse duration enters the few-cycle regime, additional parameters may influence the scattering dynamics,[20] and the scattering process can be treated as a multi-mode problem[27] that will be addressed in the future. Through this study, we reveal the physical mechanism behind ADF and identify its connection to electron motion. We employ a generalized phased Bessel (GPB) function to account for the probability amplitude associated with multiphoton process, including its magnitude and phase.

2. Transition matrix element and rate formula

The nonlinear scattering process is typically addressed within the framework of Furry picture, wherein the interaction between the intense laser field and an electron is treated rigorously, while the interaction involving the scattered photon with both the electron and laser field is perturbatively treated. This has been extensively explored in QED textbook[28] and related literatures.[20,29,30]

By employing the quantum-field Volkov state derived by Guo *et al.*,[26,31] we derive the transition matrix element for relativistic electron scattering in the presence of intense laser fields. Owing to the distinct treatment of the bispinor, the averaging operation over spin states is significantly simplified. The rate of photon emission with four-momentum k' is worked out to be (the natural unit $\hbar = c = 1$ is employed throughout this paper)

$$\frac{\mathrm{d}^2 W}{\mathrm{d}\omega' \mathrm{d}\Omega_{k'}} = \frac{\omega'(2\pi)^5}{m_\mathrm{e}^2} |\tilde{T}_\mathrm{fi}|^2, \tag{1}$$

where $\mathrm{d}\Omega_{k'} = \sin\theta \mathrm{d}\theta \mathrm{d}\phi$ is the differential solid angle of k' with θ and ϕ being scattering and azimuthal angles, respectively, and the Doppler shifted frequency is given by

$$\omega' = \frac{j_0 Pk}{P\hat{n}' + (u_p + j_0)k\hat{n}'}, \tag{2}$$

which is obtained by the energy–momentum conservation, $\hat{n}' = k'/\omega'$, $u_\mathrm{p} = e^2\Lambda^2/(kP)$ with 2Λ being the classical amplitude of vector potential and P the electron four momentum before scattering, and j_0 denotes the number of transferred photons during scattering. When $kk' \ll kP$, $\tilde{T}_\mathrm{fi}$ is given by

$$\begin{aligned} \tilde{T}_\mathrm{fi} &= |e|\Lambda[\mathcal{X}_{j_0-1}(\varsigma,\eta)\epsilon\epsilon'^{*} + \mathcal{X}_{j_0+1}(\varsigma,\eta)\epsilon^{*}\epsilon'^{*}] \\ &\quad + \mathcal{X}_{j_0}(\varsigma,\eta)^{*} P\epsilon'^{*}, \end{aligned} \tag{3}$$

where e and m_e denote the charge and rest mass of an electron, respectively; and ϵ the four polarization vector of the laser field. The scalar product $\epsilon\epsilon'^{*} = -\boldsymbol{\epsilon}\cdot\boldsymbol{\epsilon}'^{*}$, where $\boldsymbol{\epsilon} = (1,0,0)$ and $\boldsymbol{\epsilon}'$ denoting the polarization vector of the scattered photon and is chosen as $\boldsymbol{\epsilon}'_1 \cdot \boldsymbol{k}' = 0$ and $\boldsymbol{\epsilon}'_2 = \boldsymbol{\epsilon}'_1 \times \boldsymbol{k}'$. The GPB functions in Eq. (3) are defined as

$$\mathcal{X}_j(z_\mathrm{c}, z_s) = \sum_{m=-\infty}^{\infty} X_{j-2m}(z_\mathrm{c}) X_m(z_s), \tag{4}$$

in which the phased Bessel function is defined as $X_n(z) = \mathrm{J}_n(|z|)\exp(\mathrm{i}n\arg(z))$ where $\mathrm{J}_n(|z|)$ is the Bessel function and z is an ordinary complex number. The arguments of GPB functions are given by

$$\begin{aligned} \varsigma &= \frac{2|e|\Lambda}{kP}\boldsymbol{P}\cdot\epsilon - \frac{2|e|\Lambda}{kP'}\boldsymbol{P}'\cdot\epsilon, \\ \eta &= \frac{1}{2}\left(\frac{e^2\Lambda^2}{kP} - \frac{e^2\Lambda^2}{kP'}\right)\epsilon\cdot\epsilon, \end{aligned} \tag{5}$$

where P and P' are the on-shell four momentum of electron before and after scattering, respectively. The GPB functions satisfy the addition, subtraction, and recurrence theorems in both the complex range and complex domain,[32] which has been used to simplify the transition matrix element. In the above formulas, the scalar product of two four-vectors is defined as $ab = a_0 b_0 - \boldsymbol{a}\cdot\boldsymbol{b}$.

The transition matrix element in Eq. (3) indicates that the scattered photons arise from two distinct sources: one is associated with the electron-harmonic interaction, while the other is linked to the laser-harmonic interaction. This features stems from the minimal-coupling principle and highlights the different contributions of the electron momentum P and the vector potential A of the laser field.

3. Evolution of angular-resolved scattering rate

We calculate the ADFs under various conditions, based on the aforementioned formula. The angular resolved rates record a direct measure of the scattering rate and its shape

indicates the relative variation with azimuthal angle. Studying the angular resolved rates offers a convenient tool for elucidating the underlying variation mechanism under identical conditions. Following the first observation on several low-order harmonics in the Thomson scattering,[10] significant attention was drawn towards the angular resolved rates, leading to subsequent continuous observations reported under various conditions.[9,21–23] In this paper, we provide a comprehensive analysis of the ADFs. The discussion on the harmonics is presented in Ref. [25].

Firstly, to demonstrate the dipole emission characteristics, we conduct calculations of ADFs under conditions of low laser intensity and slow electron motion. In a linearly polarized laser field, the induced dipole momentum oscillates along the polarization direction, resulting in a toroidal strength distribution around it. The calculated ADFs in *xoy* plane and *xoz* plane, illustrated in Fig. 1, exhibit a figure-8 variation pattern, while that in *yoz* plane remains constant regardless of angle variations. This figure-8 pattern indicates that photons are predominantly emitted perpendicular to the laser polarization, while less radiation is emitted along its polarization axis. A three-dimensional (3D) plot is shown in plot (d), which exhibits the known donut structure of dipole emission. These features hold true for slow electrons, in which the relativistic effect is weak. These features align with those observed in dipole emission.

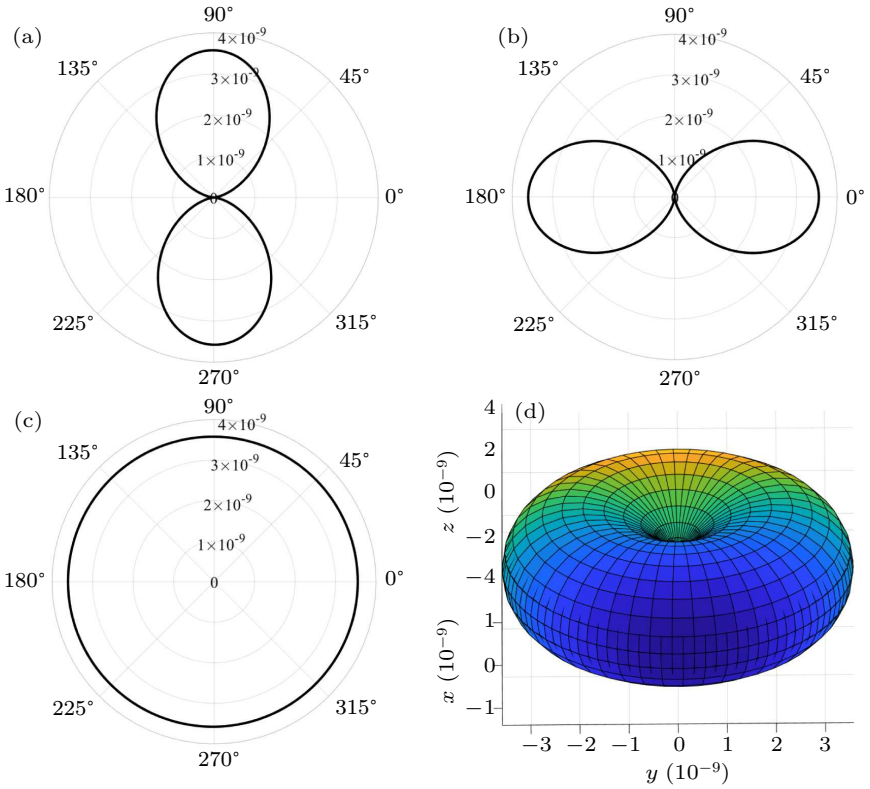


Fig. 1. Polar plots depicting the ADFs in (a) *xoy* plane, (b) *xoz* plane, and (c) *yoz* plane, respectively. (d) A three-dimensional (3D) plot of the ADF. The laser field is linearly polarized along *x*-axis and of intensity 1.0×10^{16} W/cm^2 and wavelength 800 nm. The electron moves along negative *z*-axis with magnitude 0.01, measured in the unit of $m_e c$.

Secondly, we focus on the emission in *xoy* plane to display the evolution of ADFs with respect to electron momentum and laser intensity. As the electron momentum gradually increases, significant changes occur in the ADFs corresponding to different electron momenta. Figure 2(a) presents the ADF calculated at 1.0×10^{18} W/cm^2 for various electron momenta. The black curves depict the ADF calculated under conditions similar to a recent experiment.[22] While maintaining its figure-8 like pattern, a detailed comparison reveals slight deviations of maximal rates from the vertical line, consistent with observations reported in Ref. [22]. This deviation results in the left-right asymmetry in the polar plot. The asymmetry and deviation from the vertical line become more pronounced as electron momentum increases, as illustrated by the red and blue curves in panel (a). Due to each ADF retaining its figure-8 pattern but exhibiting increasing notable deviations from the vertical alignment for maximum values, it appears as if the ADF is rotating anti-clockwise with increasing electron momentum.

The rotation of ADFs is also dependent on the laser intensity. The figure-8 profiles are almost identical at various laser intensities, but the orientation varies with the laser intensity. Figure 2(b) illustrates the ADFs calculated at various laser intensities for $|\boldsymbol{P}|$ =2.5. It is evident that as laser intensity increases, the ADF rotates clockwise. At a laser intensity about 1.0×10^{22} W/cm^2, the ADF returns to the vertical direction and regains left-right symmetry. This indicates an inverse relationship between laser intensity and electron mo-

mentum in influencing the behavior of ADFs. To achieve similar ADF patterns, one can either increase laser intensity or decrease electron momentum accordingly. A scaling law for ADF states that identical patterns can be obtained by maintaining a constant ratio between laser intensity and electron energy.

The scattering dynamics of electrons in intense laser fields are determined by the GPB functions, including their order and arguments. The change in the calculated ADF with laser intensity and electron momentum can be easily interpreted from this perspective. In the transition matrix element given by Eq. (3), three GPB functions with different weights contribute to one ADF. Both the GPB functions and their weights vary with laser intensity and electron momentum, thus the contribution of each term in Eq. (3) to the overall scattering rate depends on these two factors. Specifically, the weights of $\mathcal{X}_{j_0\pm1}$ terms increase with laser intensity, while that of $\mathcal{X}_{j_0}$ term increases with electron momentum. These three terms exhibit different variations with respect to azimuthal angle, as illustrated in Fig. 3. By comparing magnitude among these three terms, we conclude that j_0-1 and j_0 terms mainly contribute to ADF. Due to their distinct dependence on azimuthal angle, their coherent overlapping results in a deviation from vertical direction for maximum value of ADF depicted in panel (a). When either laser intensity or electron momentum change, their weights changes and hence the orientation of maximum scattering rate varies accordingly. However, when the ratio of laser intensity to electron energy remains constant, the ADF remains unchanged, and hence a scaling law is established.

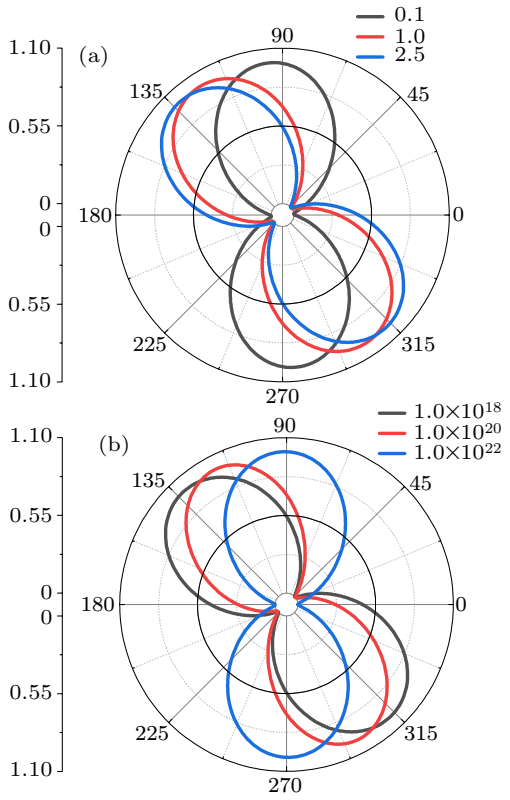


Fig. 2. Polar plots depicting the ADFs in the *xoy* plane for (a) laser intensity 1.0×10^{18} W/cm^2 but different electron momenta, and (b) electron momentum 2.50 but different laser intensities, respectively. The laser field is polarized along x-axis and propagates along z-axis. The laser wavelength is 800 nm. The electron moves along negative z-axis with magnitude measured in the unit of m_ec.

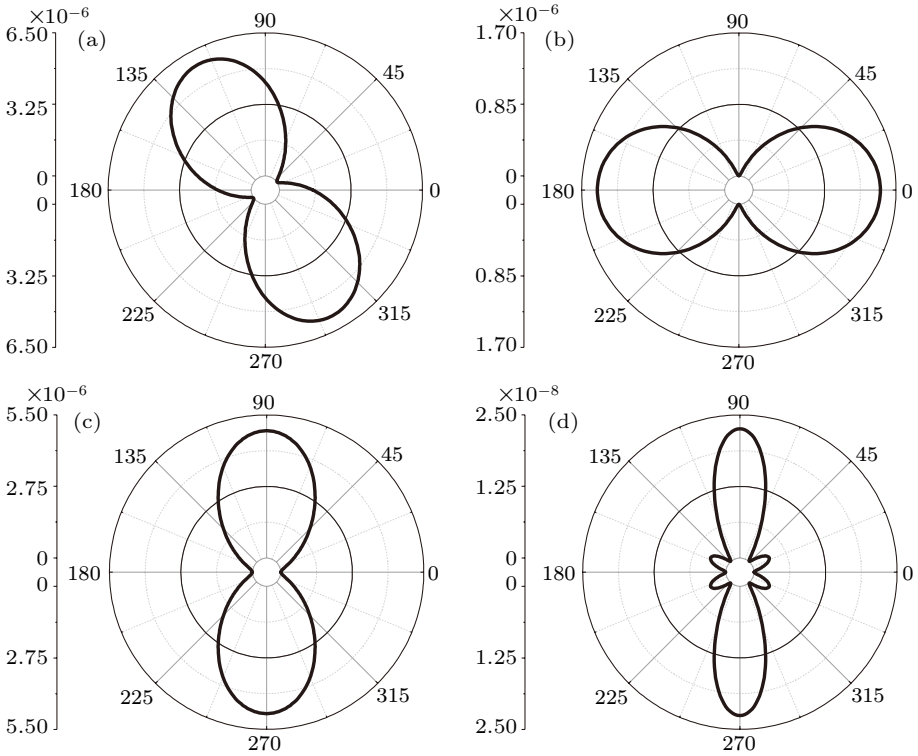


Fig. 3. Polar plots of ADF in the *xoy* plane (a) and variation of $|\mathcal{X}_{j_0-1}|^2$ (b), $|\mathcal{X}_{j_0}|^2$ (c), and $|\mathcal{X}_{j_0+1}|^2$ (d) with the azimuthal angle, respectively. Calculations are performed for electron momentum 1.2 and laser intensity 1.0×10^{19} W/cm^2.

Next, we investigate the radiation rate in *yoz* plane and focus on how it varies with θ under different conditions. In a head-on collision where the electron moves along negative z-axis, $\boldsymbol{P}\cdot\epsilon = 0$ resulting in $\varsigma = 0$ for emission in *yoz* plane. Consequently, the transition matrix element can be simplified to

$$\tilde{T}_{\rm fi} = |e|\Lambda[X_0(\eta)\epsilon\epsilon'^{*} + X_1(\eta)\epsilon^{*}\epsilon'^{*}], \tag{6}$$

where $\boldsymbol{\epsilon}'$ is taken as $(1,0,0)$. The variation of ADF is primarily influenced by η's dependence on the scattering angle θ through the Doppler shifted frequency in ω' given by Eq. (2). It is then natural to observe that at lower laser intensities and for small electron momenta where the Doppler effect is negligible, the emission rate in *yoz* plane remains independent of θ, resulting in isotropic ADFs, as depicted in Fig. 1(c). However, as laser intensity and/or electron momentum increases and the Doppler effect becomes dominant, the ADF loses its isotropy gradually.

The ADFs calculated at 1.0×10^{18} W/cm^2 for various electron momenta are illustrated in Fig. 4. It is evident that the ADFs are currently non-isotropic, displaying a maximum and a minimum located along the z-axis. As electron momentum increases, the maximum value increases while the minimum tends to zero. Consequently, for higher electron momenta, the ADF becomes more orientated due to the noticeable Doppler effect caused by high-speed electrons. This trend is depicted in Fig. 4(d) for $|\boldsymbol{P}|$ =10.0, where the ADF exhibits a pronounced peak at $\theta = 180°$, indicating that backscattering dominates the scattering process when the electron momentum is large. These changes are mainly determined by $X_0(\eta)$ in expression (6).

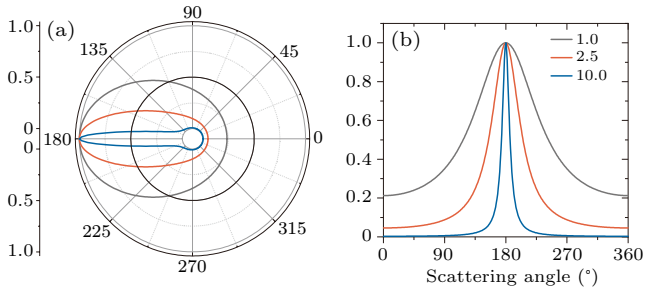


Fig. 4. Panel (a) shows the ADFs in the *yoz* plane, and panel (b) shows variation of $|X_0|^2$ with the scattering angle θ. Black/red/blue curves are for electron momentum 1.0, 2.5, and 10.0, respectively. The laser intensity is taken as 1.0×10^{18} W/cm^2, respectively.

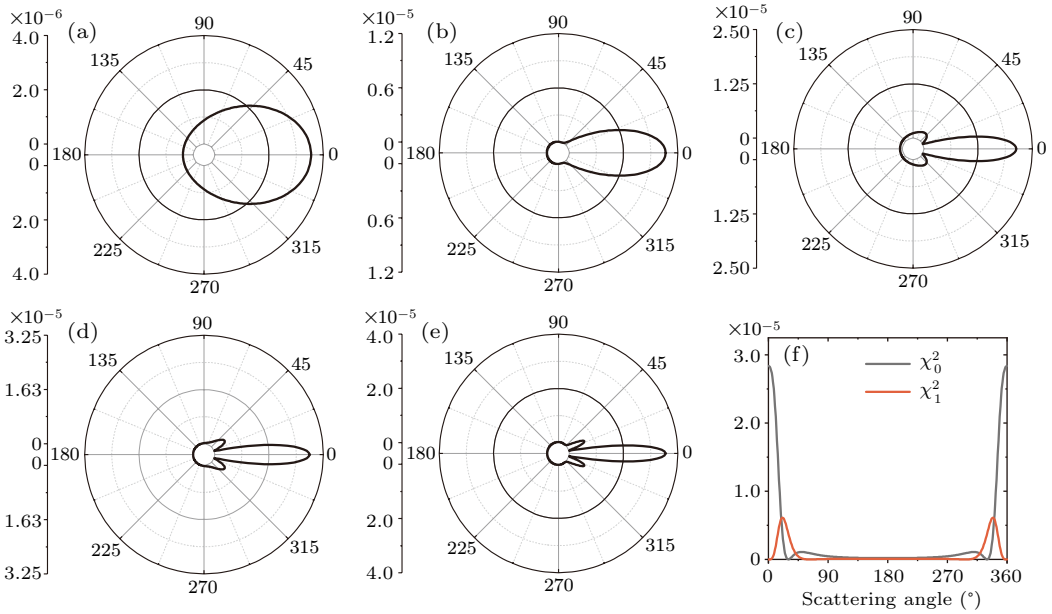


Fig. 5. Polar plots of the ADFs in the *yoz* plane calculated for electron momentum $|\boldsymbol{P}| = 0.1$ at different laser intensities: (a) 1.0×10^{19} W/cm^2, (b) 3.0×10^{19} W/cm^2, (c) 6.0×10^{19} W/cm^2, (d) 8.0×10^{19} W/cm^2, (e) 10.0×10^{19} W/cm^2, respectively. Each ADF denotes the variation of radiation rate with scattering angle θ. Panel (f) displays the variation of $|X_1|^2$ and $|X_0|^2$ with the scattering angle θ.

The ADFs calculated at different laser intensities for the electron momentum $|\boldsymbol{P}| = 0.1$ are depicted in Fig. 5. As the laser intensity increases, the ADFs become highly peaked along the laser propagation direction, exhibiting anisotropic behavior. These features can be well explained by considering the properties of Bessel functions and their variation with respect to the scattering angle θ. The value of η firstly increases with θ and then reaches a broad platform region before rapidly decreasing, displaying a trapezoidal-like variation pattern. The maximum value of η increases with laser intensity but decreases with electron momentum. Consequently, in higher intensity laser fields, there is a rapid change in η with θ at both rising and falling edges. This change determines the pattern of ADF and its variation with laser intensity. At lower laser intensities where η is small, $X_0(\eta)$ dominates the ADF profile, resulting in a fat elliptical shape, as shown in Figs. 5(a) and 5(b). However, as laser intensity increases and thus leads to an increase in maximum value of η, there

is a swift decrease in $X_0(\eta)$ which causes gradual narrowing down of the elliptical distribution until it resembles a sharp peak. Therefore, higher laser intensity results in sharper lobe structure. When the maximum value of η exceeds the first zero point of $X_0(\eta)$, two non-emission points appear at $\pm 30^\circ$ in Fig. 5(c). Between these two points (from 30° to 330°), an arc-like distribution appears due to slow variation of $X_0(\eta)$ in η's flat top region. Plots (d) and (e) display how a pair of side jets are generated beside the sharp peak structure. These side jets indicate contribution from $X_1(\eta)$ term, as shown in plot (f) for laser intensity 1.0×10^{20} W/cm^2. As η increases with θ, $X_1(\eta)$ firstly increases and then starts decreasing again, leading to the formation of jet-like structure within ADF profile. The interference between the two terms slightly changes θ's value corresponding to the top of jets.

A comparison between Figs. 4(a) and 5(a) clearly illustrates the contrasting effects of electron momentum and laser intensity in head-on collisions. Based on this comparison, it can be inferred that increasing laser intensity promotes the emission of scattered photons along the direction of laser propagation, while high-energy incident electrons push more photons to be emitted in the opposite direction. If both the laser intensity and the electron momentum are adjusted proportionally, the scattering dynamics will remain unchanged, leading to equivalent ADFs. An example is presented in Fig. 6, which demonstrates that equivalent ADFs are obtained when the electron momentum is enlarged by n times and the laser intensity is enlarged by n^2 times. In this manner, both the ratio of weights in Eq. (3), say $|e|\Lambda/|P|$ and the arguments of GPB functions in Eq. (5) remain constant.

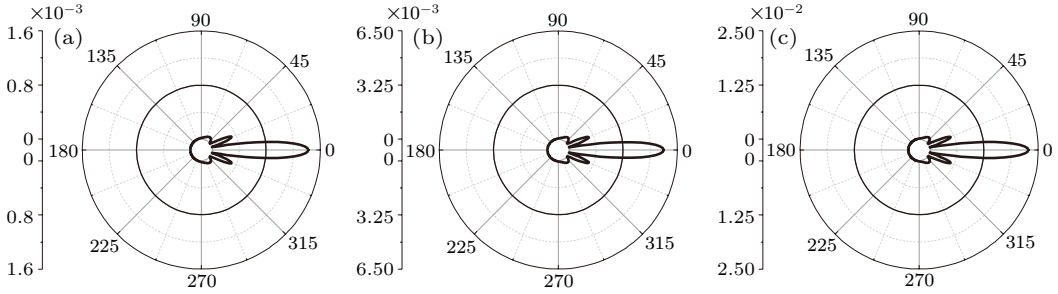


Fig. 6. Polar plots of the ADFs calculated at (a) $I=4.0\times10^{21}$ W/cm^2, $p_0=4.0$; (b) $I=1.6\times10^{22}$ W/cm^2, $p_0=8.0$; (c) $I=6.4\times10^{22}$ W/cm^2, $p_0=16.0$.

Finally, we investigate the influence of relativistic effect on the scattering dynamics, by comparing the calculated ADFs with those obtained in the non-relativistic (NR) limit. In the NR limit, we have $kP\to m_e\omega$ and $kP'\to m_e\omega$ and hence the arguments of GPB functions reduce to

$$\begin{aligned}\varsigma &= \frac{2|e|\Lambda}{m_e\omega}\boldsymbol{k}'\cdot\epsilon = \frac{2|e|\Lambda}{m_e\omega}\omega'\sin\theta\cos\phi,\\ \eta &= \frac{1}{2}\left(\frac{e^2\Lambda^2}{m_e\omega}-\frac{e^2\Lambda^2}{m_e\omega}\right)\epsilon\cdot\epsilon = 0,\end{aligned}\tag{7}$$

and the Doppler shifted frequency is given by

$$\omega' = \frac{j_0 m_e\omega}{m_e+(u_p+j_0)\omega}.\tag{8}$$

For the radiation in yoz plane, where $\phi=0$ and $\varsigma=0$, the transition matrix element in Eq. (6) remains constant in all directions, and the emission rate is modulated by the Doppler effect via the dependence of ω'. This suggests that the observed variation of ADFs with θ is caused by the relativistic effect induced by the laser intensity and the electron motion. The greater the asymmetry in ADFs, the stronger these relativistic effects become. For the radiation in xoy and xoz planes, we seek for the numerical comparison.

The comparison of the calculated ADFs in Fig. 7 clearly illustrates the significant influence of relativistic effects on radiation rate in different directions. In xoy plane, relativistic effects lead to a reduction in radiation rate and retard the rotation of ADFs. In xoz plane, the ADFs exhibit a distorted figure-8 profile, with relativistic effect amplifying this distortion. Additionally, due to relativistic effects, the emission rate in the xoz plane is lower compared to NR cases. In the yoz plane, the ADFs assume an elliptical profile where relativistic effects decrease emission rate and give rise to other aforementioned phenomena. A common feature is that the relativistic effects decrease the radiation rate in various directions, which is due to the electrons' fast motion sharing more energy of the entire interacting system.

Surprisingly, the ADF treated with NR limit in the xoy plane, as depicted in Fig. 7(a), also exhibit a rotation away from the vertical line. This implies that even when neglecting relativistic effects, the maximal emission rate does not align vertically with the laser polarization. This phenomena deviate from the typically characteristics of the diploe emission. The observed rotation indicates that for high-speed electrons, there is a notable contribution from j_0 term in Eq. (3), which varies with the azimuthal in a pattern as shown in Fig. 3(b). As the laser intensity increases, clockwise rotation occurs for NR-treated ADFs.

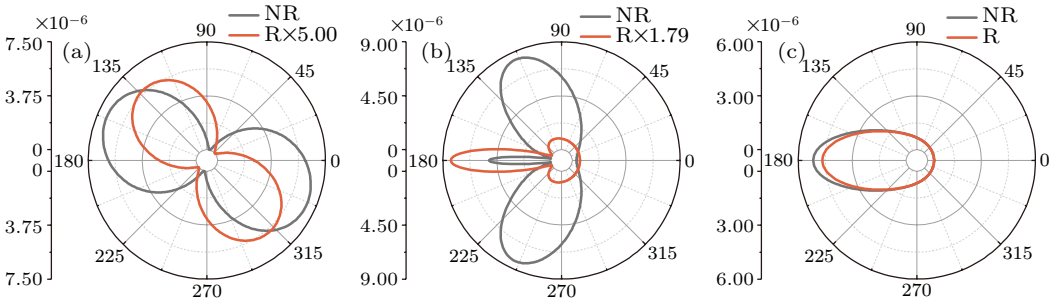


Fig. 7. Polar plots of the ADFs calculated at a laser intensity of 1.0×10^{18} W/cm^2 and electron momentum of 2.0 in (a) *xoy*, (b) *xoz*, and (c) *yoz* planes are presented. The black/red curves represent the ADFs without/with relativistic effects, respectively. To enhance clarity, the red ADHs in panels (a) and (b) have been magnified by factors of 5 and 1.79, respectively.

4. Conclusions

By employing a full quantum theory of electron–photon scattering in intense laser fields, we determine the angular-resolved radiation rates of the fundamental wave emitted through Thomson scattering under various laser intensities and electron momenta. We investigate the ADFs in *xoy*, *xoz*, and *yoz* planes and analyze their evolution with laser intensity and electron momentum. The figure-8 profile of radiation rate within the polarization plane is validated, while its dependence on laser intensity and electron momentum is illustrated. Our findings reveal that in lower-intensity laser fields and for slow electron motion, the ADFs exhibit distinct dipole emission characteristics. However, significant changes are observed when encountering high laser intensities and/or large electron momenta, leading to pronounced alterations in the ADFs. Furthermore, we elucidate the underlying physical mechanism by which a method to achieve ADFs is established through proportional adjustments of both laser intensity and electron momentum.

Acknowledgements

Project supported by the National Natural Science Foundation of China (Grant No. 12074261) and the Natural Science Foundation of Shanghai (Grant No. 20ZR1441600). The authors thank suggestive discussion with Guo D S and Chen Y Y.

References

[1] Thomson J 1899 *Philosophical Magazine and Journal of Science* **47** 253
[2] Gonoskov A, Blackburn T G, Marklund M and Bulanov S S 2022 *Rev. Mod. Phys.* **94** 045001
[3] Khrennikov K, Wenz J, Buck A, Xu J, Heigoldt M, Veisz L and Karsch S 2015 *Phys. Rev. Lett.* **114** 195003
[4] Sarri G, Corvan D J, Schumaker W, Cole J M, Di Piazza A, Ahmed H, Harvey C, Keitel C H, Krushelnick K, Mangles S P D, Najmudin Z, Symes D, Thomas A G R, Yeung M, Zhao Z and Zepf M 2014 *Phys. Rev. Lett.* **113** 224801
[5] Chi Z 2022 *Nuclear Inst. and Methods in Physics Research A* **1033** 166681
[6] Sarachii E S and Schappert G T 1970 *Phys. Rev. D* **1** 2738
[7] Esarey E, Ride S K and Sprangle P 1993 *Phys. Rev. E* **48** 3003
[8] Ride S K, Esarey E and Baine M 1995 *Phys. Rev. E* **52** 5425
[9] Babzien M, Ben-Zvi I, Kusche K, Pavlishin I V, Pogorelsky I V, Siddons D P, Yakimenko V, Cline D, Zhou F, Hirose T, Kamiya Y, Kumita T, Omori T, Urakawa J and Yokoya K 1996 *Phys. Rev. Lett.* **96** 054802
[10] Chen S Y, Maksimchuk A and Umstadter D 1998 *Nature* **396** 653
[11] Gao J 2004 *Phys. Rev. Lett.* **93** 243001
[12] Zhao S H, Lue Q Z, Yuan S Y and Li Y J 2011 *Acta Phys. Sin.* **60** 054209 (in Chinese)
[13] Yan W, Fruhling C, Golovin G, Haden D, Luo J, Zhang P, Zhao B, Zhang J, Liu C, Chen M, Chen S, Banerjee S and Umstadter D 2017 *Nat. Photon.* **11** 514
[14] Wang Y, Yang Q, Chang Y, Lin Z and Tian Y 2024 *Chin. Phys. B* **33** 013301
[15] Chang Y, Wang Y, Wang C, Shen Y and Tian Y 2023 *Chin. Phys. B* **32** 063201
[16] Tomassini Paolo, Bacci A, Cary J, Ferrario M, Giulietti A, Giulietti Danilo, Gizzi L A, Labate Luca, Serafini L, Petrillo Vittoria and Vaccarezza C 2008 *IEEE Tran. Plasma. Sci.* **36** 1782
[17] Maroli C, Petrillo V, Tomassini P and Serafini L 2013 *Phys. Rev. Spe. Top. Accerl. Beam* **16** 030706
[18] Kumita T, Kamiya Y, Babzien M, Ben-Zvi I, Kusche K, Pavlishin I V, Pogorelsky I V, Siddons D P, Yakimenko V, Hirose T, Omori T, Urakawa J, Yokoya K, Cline D and Zhou F 2010 *Laser Phys.* **16** 267
[19] Li A K, Wang J X, Ren N, Zhu W J, Li X Y, Hoehn R and Kais S 2014 *Laser Phys.* **24** 015302
[20] Heinzl T, Seipt D and Kampfer B 2010 *Phys. Rev. A* **81** 022125
[21] Shao Z, Dong Q, Teng H, Li Z, Yue D, Liu Q, Wei Z and Zhang J 2023 *Phys. Rev. A* **107** 053109
[22] Pratt B, Atkinson N, Hodge D, Romero M, Schulzke C, Sun Y, Ware M and Peatross J 2021 *Phys. Rev. A* **103** L031102
[23] Fruhling C, Wang J, Umstadter D, Schulzke C, Romero M, Ware M and Peatross J 2021 *Phys. Rev. A* **104** 053519
[24] Salamin Y I and Faisal F H M 1996 *Phys. Rev. A* **54** 4383
[25] Shen Y, Ren X and Zhang J 2025 *J. Phys A* **58** 185701
[26] Guo D S and Aberg T 1988 *J. Phys. A* **21** 4577
[27] Zhang J, Feng X, Xu Z and Guo D S 2004 *Phys. Rev. A* **69** 043409
[28] Berestetskii V, Lifshitz E and Pitaevskii L 1982 *Quantum Electrodynamics* (Course of Theoretical Physics) (Butterworth, Washington DC), Ch. 101, P437 (in Chinese)
[29] Makarov D N 2023 *Results in Physics* **52** 106790
[30] Dai D and Fu L 2022 *Phys. Rev. A* **105** 013101
[31] Guo D S and Aberg T 1991 *J. Phys. B* **24** 349
[32] Hu X, Wang H X and Guo D S 2008 *Can. J. Phys.* **86** 863